

TIME VARIABILITY IN THE X-RAY NEBULA POWERED BY PULSAR B1509–58

T. DELANEY AND B. M. GAENSLER¹

Harvard-Smithsonian Center for Astrophysics, 60 Garden Street, Cambridge, MA 02138; tdelaney@cfa.harvard.edu,
bgaensler@cfa.harvard.edu

J. ARONS

Department of Astronomy, University of California, Berkeley, CA 94720; arons@berkeley.edu

AND

M. J. PIVOVAROFF

Lawrence Livermore National Laboratory, 7000 East Avenue, Livermore, CA 94550; pivovarovf1@llnl.gov

Received 2005 August 1; accepted 2005 November 30

ABSTRACT

We use new and archival *Chandra* and *ROSAT* data to study the time variability of the X-ray emission from the pulsar wind nebula (PWN) powered by PSR B1509–58 on timescales of 1 week to 12 yr. There is variability in the size, number, and brightness of compact knots appearing within 20'' of the pulsar, with at least one knot showing a possible outflow velocity of $\sim 0.6c$ (assuming a distance to the source of 5.2 kpc). The transient nature of these knots may indicate that they are produced by turbulence in the flows surrounding the pulsar. A previously identified prominent jet extending 12 pc to the southeast of the pulsar increased in brightness by 30% over 9 yr; apparent outflow of material along this jet is observed with a velocity of $\sim 0.5c$. However, outflow alone cannot account for the changes in the jet on such short timescales. Magnetohydrodynamic sausage or kink instabilities are feasible explanations for the jet variability, with timescales of ~ 1.3 –2 yr. An arc structure located 30''–45'' north of the pulsar shows transverse structural variations and appears to have moved inward with a velocity of $\sim 0.03c$ over 3 yr. The overall structure and brightness of the diffuse PWN exterior to this arc and excluding the jet has remained the same over the 12 yr span. The photon indices of the diffuse PWN and possibly the jet steepen with increasing radius, likely indicating synchrotron cooling at X-ray energies.

Subject headings: ISM: individual (G320.4–1.2) — ISM: jets and outflows — pulsars: individual (B1509–58) — stars: neutron — supernova remnants — X-rays: ISM

1. INTRODUCTION

The pulsar B1509–58 and the supernova remnant (SNR) G320.4–1.2 (MSH 15–52) represent one of approximately 20 known associations between a pulsar and a SNR. This pulsar is one of the most energetic known, with a period (P) of 150 ms, a period derivative (\dot{P}) of $1.2 \times 10^{-12} \text{ s s}^{-1}$, a characteristic age $\tau_c \equiv P/2\dot{P} \approx 1700 \text{ yr}$, a spin-down luminosity $\dot{E} \equiv 4\pi^2 I \dot{P} P^{-3} \approx 1.8 \times 10^{37} \text{ ergs s}^{-1}$ (for a moment of inertia $I \equiv 10^{45} \text{ g cm}^2$), and an inferred dipole surface magnetic field $B_p \approx 3.2 \times 10^{19} (P\dot{P})^{1/2} \approx 1.5 \times 10^{13} \text{ G}$ (Kaspi et al. 1994; Livingstone et al. 2005).

SNR G320.4–1.2 has been well studied at radio, optical, and X-ray wavelengths. The radio morphology consists of a partial shell to the southeast and a series of bright clumps $\sim 25'$ to the northwest (Gaensler et al. 1999) that coincide with the optical nebula RCW 89 (Rodgers et al. 1960; Seward et al. 1983). The X-ray morphology consists of a bright, elongated pulsar wind nebula (PWN) with a collimated jet extending $\sim 4'$ to the southeast (Seward et al. 1983; Greiveldinger et al. 1995; Trussoni et al. 1996; Brazier & Becker 1997; Gaensler et al. 2002, hereafter G02). To the northwest are thermal clumps associated with the radio clumps and RCW 89 (Seward et al. 1983). In addition, G02 identified several compact knots close to the pulsar, plus two semicircular arcs at a distance of 17'' and 30'' to the north of the pulsar. The toroidal morphology and collimated jet are reminiscent of structures found in the PWNe powered by the Crab

and Vela pulsars (Hester et al. 1995; Weisskopf et al. 2000; Helfand et al. 2001). The arcs have been proposed as being due to ion compression in the particle-dominated equatorial flow from the pulsar and were interpreted by G02 as analogs of the “wisps” found in the Crab Nebula. SNR G320.4–1.2 has recently been observed in very high energy γ -rays by the High Energy Stereoscopic System (HESS). The emission is elongated along the PWN axis, possibly indicating inverse Compton scattering of relativistic electrons (Aharonian et al. 2005).

The structures in the Crab and Vela PWNe are known to vary in brightness and position over short timescales (from days to months). In the case of the Crab Nebula, the outward-moving X-ray and optical wisps (with velocity $v \sim 0.5c$) are thought to mark the PWN termination shock, while the small-scale X-ray and optical knots are thought to identify unstable, quasi-stationary shocks in the pulsar wind (Hester et al. 2002). Radio wisps, which rarely correspond to optical wisps, develop and move outward at slower velocities ($v \sim 0.3c$), and there are even more slowly moving radio features ($v \sim 10^4 \text{ km s}^{-1}$) farther away from the pulsar (Bietenholz et al. 2004). Recent observations of the wisps and polar knots in the near-infrared indicate brightness variations on timescales as short as 20 minutes (Melatos et al. 2005). In the case of the Vela PWN, the X-ray arcs also move outward and vary in brightness by up to 30% (Pavlov et al. 2001).

The variability of the Vela PWN jet observed in X-rays has been attributed to both kink instabilities, which would account for the dramatic shape and the brightness changes over the

¹ Alfred P. Sloan Research Fellow.

course of days, and sausage instabilities, which would account for the relativistically moving “blobs” ($v \sim 0.5c$; Pavlov et al. 2003). The Crab Nebula jet, on the other hand, shows only weak X-ray morphological variations on year-long timescales (Mori et al. 2004b) and relativistic outflow identified in the optical with $v \sim 0.4c$ (Hester et al. 2002).

The PWN powered by PSR B1509–58 represents a unique opportunity to study variability in PWNe. The physical size of the PWN is approximately 10 and 100 times larger than the Crab and Vela PWNe, respectively. Given the observed variability in the Crab and Vela PWNe and the distance to PSR B1509–58 (5.2 ± 1.4 kpc; Gaensler et al. 1999), G02 predicted measurable variability in the PWN of PSR B1509–58 on timescales of a few years. To that end, we obtained new *Chandra* observations of PSR B1509–58 and its PWN. In this paper we compare our new images to existing *ROSAT* PSPC and HRI images and *Chandra* ACIS-I images and report on the variations observed over timescales of 1 week to 12 yr.

2. X-RAY OBSERVATIONS AND ANALYSIS

We observed G320.4–1.2 with the *Chandra* Advanced CCD Imaging Spectrometer (ACIS-I) detector on 2003 April 21 for a total of 9.6 ks, on 2003 April 28 for a total of 10 ks, and on 2003 October 18 for a total of 19.4 ks. The data were calibrated using CIAO version 3.1 and CALDB version 2.28. After filtering for good time intervals, the total usable exposure times were 9469, 9497, and 18739 s for the April 21, April 28, and October 18 observations, respectively. Exposure-corrected images were constructed for each epoch between 0.3 and 8 keV, as outlined in G02. The telescope was not dithered during the 2003 April 28 observation, so the effects of the chip gaps and dead columns could not be removed at that epoch.

G320.4–1.2 had been previously observed with the *Chandra* ACIS-I detector on 2000 August 14 for a total of 19.3 ks (G02). The archival data products were obtained from the *Chandra* archive and were recalibrated using CIAO version 3.1 and CALDB version 2.28 to make use of the newest gain solutions and to correct the geometry of the data set.² The data were filtered for good time intervals, resulting in a final exposure time of 17,863 s, and an exposure-corrected image was made as outlined above.

We compare these *Chandra* data to archival observations with the *Röntgensatellit* (*ROSAT*; Trümper 1982; Pfeiffermann et al. 1987). G320.4–1.2 was observed with the *ROSAT* Position Sensitive Proportional Counter (PSPC) detector on 1991 February 22–March 8 and 1992 February 25–27 for a total of 9.1 ks (Greiveldinger et al. 1995; Trussoni et al. 1996). Data were also taken with the *ROSAT* High Resolution Imager (HRI) detector on 1994 February 10–23 and 1994 September 15 for a total of 22.5 ks (Brazier & Becker 1997). The archival data products were obtained from NASA’s HEASARC.³ Exposure-corrected images were made using the Xselect utility and the `hr1expmap` and `pcexpmap` tasks within version 5.3.1 of the FTOOLS package. The exposure times of the PSPC and HRI data are approximately matched to produce the same number of counts on the two images. To facilitate comparison to the *Chandra* images, exposure-corrected images were also made from 2 ks each of the 2000 August 14 and 2003 October 18 *Chandra* data sets to match

the energy range (~ 0.1 – 2.5 keV) and the number of counts⁴ on the *ROSAT* PSPC and HRI images.

The four *Chandra* images were registered to each other using a brightness-weighted mean of PSR B1509–58, the star Muzzio 10 (located at [J2000.0] R.A. = $15^{\text{h}}13^{\text{m}}55^{\text{s}}.2$, decl. = $-59^{\circ}07'51''.6$; Muzzio 1979), and four other background sources in the field (located at [J2000.0] R.A. = $15^{\text{h}}13^{\text{m}}41^{\text{s}}$, decl. = $-59^{\circ}11'45''$; R.A. = $15^{\text{h}}14^{\text{m}}00^{\text{s}}$, decl. = $-59^{\circ}12'38''$; R.A. = $15^{\text{h}}14^{\text{m}}05^{\text{s}}$, decl. = $-59^{\circ}14'40''$; and R.A. = $15^{\text{h}}14^{\text{m}}32^{\text{s}}$, decl. = $-59^{\circ}08'09''$). The relative registration error is $<0''.1$, with rotation constrained to $<1^{\circ}$. Although the pulsar does not have a significant proper motion ($\mu_{\alpha} < 39$ mas yr⁻¹, $\mu_{\delta} < 52$ mas yr⁻¹; Gaensler et al. 1999), its suitability for registration purposes is in question because the strong pileup enhances the azimuthal brightness asymmetry that results from a misalignment of the telescope mirrors in the innermost shell (Jerius et al. 2000; Pavlov et al. 2001). Therefore, we also determined the registration solution excluding the pulsar. Again using a brightness-weighted mean, we find a relative registration error $<0''.1$ for the 2000 August 14 and 2003 October 18 images and $<0''.25$ for the two 2003 April images.

Spectra were extracted for selected sources of interest using the FTOOLS Xselect utility for the *ROSAT* PSPC data and the CIAO `acis-spec` script for the *Chandra* data. Background spectra were extracted from an annular region surrounding each source of interest. The spectra were rebinned to have a minimum of 20 counts per spectral channel. XSPEC version 11.3.1 was used for the spectral analysis. Unless otherwise noted, we present the 90% confidence limit for errors. All physical size and distance calculations assume that the source is 5.2 kpc away (Gaensler et al. 1999).

3. SUMMED CHANDRA IMAGE

Shown in Figure 1 is a summed and exposure-corrected image of 50 ks of the *Chandra* data, *excluding* the 2003 April 28 observation, which was not dithered. The energy range is 0.3–8.0 keV, and the image has been convolved with a Gaussian of FWHM $10''$. The pulsar position is indicated by the white plus sign. In addition to the jet and the inner and outer arcs (G02 features “C,” “5,” and “E,” respectively), we identify two faint arclike structures at distances of $\sim 110''$ and $160''$ from the pulsar. These newly identified features are labeled as “arc a” and “arc b” in the figure and are $\sim 20''$ in width. Arc a can be identified in the individual 20 ks 2000 August and 2003 October images and also appears in more recent *Chandra* images (P. Slane 2005, private communication). The newer *Chandra* data will require more analysis before we can determine whether arc b is also a robust structure.

4. TIME EVOLUTION

4.1. Flux of the Diffuse PWN

To determine whether the total flux of the diffuse PWN varied over time, we performed simultaneous absorbed power-law fits to the *ROSAT* PSPC and *Chandra* data sets, requiring the same absorbing column (N_{H}) and photon index (Γ) for all data sets, but allowing the normalization to vary between epochs (to account for both calibration uncertainties and actual, evolutionary brightness variations). We define the *diffuse* PWN to be the low-brightness

² For standard ACIS data preparation, see http://cxc.harvard.edu/ciao/guides/acis_data.html. For information on the geometry correction, see <http://cxc.harvard.edu/cal/Hrma/optaxis/platescale>.

³ See <http://heasarc.gsfc.nasa.gov/>.

⁴ Version 3.6a of the PIMMS program (<http://cxc.harvard.edu/toolkit/pimms.jsp>) was used to determine the *Chandra* exposure time needed to match the number of counts on the *ROSAT* image for the diffuse PWN and knots in the RCW 89 region.

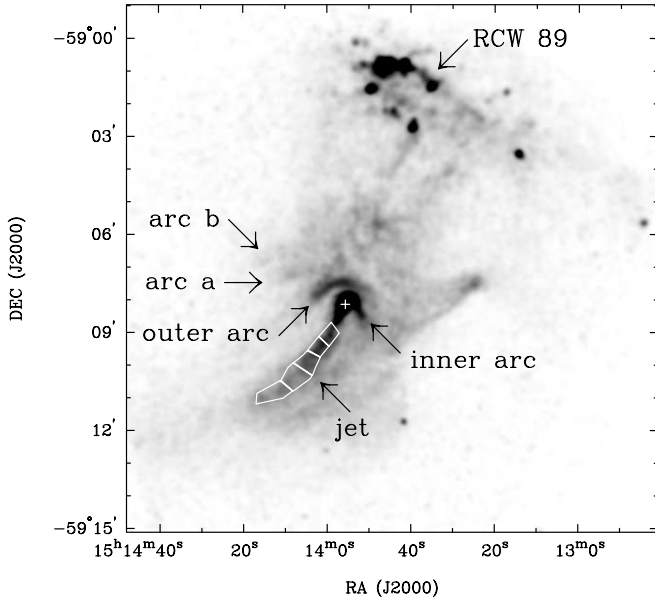


FIG. 1.—Summed 50 ks *Chandra* image of G320.4–1.2 over the energy range 0.3–8.0 keV. The image has been exposure-corrected and convolved with a Gaussian of FWHM 10". The transfer function is linear. On this and subsequent images, the pulsar position is indicated by the white plus sign. Overlaid on the jet are the regions used to determine the radial variation of the photon index, as indicated in Table 3 and the Alfvén crossing times, as indicated in Table 4.

emission surrounding the pulsar, interior to the RCW 89 region to the northwest and extending slightly beyond the jet to the southeast. We specifically exclude the jet and the inner and outer arc structures from this definition. The exact region used for the analysis is the same as that shown in Figure 7 of G02. The best-fit values are $N_{\text{H}} = (8.6 \pm 0.2) \times 10^{21} \text{ cm}^{-2}$ and $\Gamma = 1.97 \pm 0.03$. Table 1 shows the unabsorbed fluxes obtained from the simultaneous spectral fit for the energy range 0.5–10.0 keV.⁵ Note that the loss of dithering for the 2003 April 28 observation resulted in lower flux values for the diffuse PWN and jet. The total unabsorbed flux of the diffuse PWN has remained steady at $\approx 5.8 \times 10^{-11} \text{ ergs cm}^{-2} \text{ s}^{-1}$ from 1991/1992 to 2003.

The value of the absorbing column does not match that of G02 within the errors. We fitted just the recalibrated 2000 data set studied by G02 and found $N_{\text{H}} = (8.2 \pm 0.3) \times 10^{21} \text{ cm}^{-2}$ and $\Gamma = 1.91 \pm 0.04$, which is consistent with the multiepoch fit. We also fixed N_{H} at $9.5 \times 10^{21} \text{ cm}^{-2}$ and Γ at 2.05 (as found by G02) to determine what, if any, difference there is in total flux. For the energy range 0.5–10.0 keV, we obtained an unabsorbed flux of $5.8 \times 10^{-11} \text{ ergs cm}^{-2} \text{ s}^{-1}$ for both sets of values for the absorbing column and the photon index, indicating that these parameters are sufficiently degenerate that the slightly different

⁵ Although the *ROSAT* PSPC data do not extend above 2.5 keV, fluxes were extrapolated up to 10 keV using a model spectrum with the same photon index and normalization found from the spectral fits.

TABLE 1
SPECTRAL FITS TO VARIOUS SUBREGIONS OF THE SOURCE

Region	Fit ^a	Observation ^b	Epoch	Γ	F_{X}^{c} ($10^{-12} \text{ ergs cm}^{-2} \text{ s}^{-1}$)
Diffuse PWN.....	S	R	1991/1992	1.97 ± 0.03	57 ± 3
	S	C	2000 Aug 14	...	58 ± 3
	S	C	2003 Apr 21	...	58 ± 3
	S	C	2003 Apr 28 ^d	...	53 ± 3
	S	C	2003 Oct 18	...	58 ± 3
	I	C	2000 Aug 14	1.97 ± 0.03	58 ± 3
	I	C	2000 Apr 21	1.98 ± 0.03	59 ± 3
	I	C	2003 Apr 28 ^d	1.96 ± 0.03	53 ± 3
	I	C	2003 Oct 18	1.96 ± 0.03	58 ± 3
Jet.....	S	R	1991/1992	1.64 ± 0.07	4.1 ± 1.0
	S	C	2000 Aug 14	...	5.5 ± 0.6
	S	C	2003 Apr 21	...	5.2 ± 1.0
	S	C	2003 Apr 28 ^d	...	4.1 ± 1.0
	S	C	2003 Oct 18	...	5.4 ± 0.6
	I	C	2000 Aug 14	1.62 ± 0.11	5.5 ± 0.6
	I	C	2003 Apr 21	1.53 ± 0.11	5.3 ± 1.0
	I	C	2003 Apr 28 ^d	1.79 ± 0.13	4.0 ± 1.0
	I	C	2003 Oct 18	1.65 ± 0.11	5.4 ± 0.6
Outer Arc.....	S	R	1991/1992	1.64 ± 0.09	4.4 ± 1.0
	S	C	2000 Aug 14	...	3.7 ± 0.6
	S	C	2003 Apr 21	...	3.4 ± 1.0
	S	C	2003 Apr 28	...	3.3 ± 1.0
	S	C	2003 Oct 18	...	3.5 ± 0.6

NOTES.—Uncertainties are all at 90% confidence. The models used are power laws of the form $f_E \propto E^{-\Gamma}$, where Γ is the photon index and the integrated flux is $F_{\text{X}} \equiv F(E_1, E_2) = \int_{E_1}^{E_2} E f(E) dE$. All models assume interstellar absorption using the cross sections of Bałucińska-Church & McCammon (1992), assuming solar abundances.

^a Here “S” indicates the results of simultaneous fits to multiepoch data requiring the same Γ , holding N_{H} fixed at $8.6 \times 10^{21} \text{ cm}^{-2}$ and allowing the normalization to vary between epochs as outlined in § 4.1, and “I” indicates a fit to an individual epoch, holding N_{H} fixed at $8.6 \times 10^{21} \text{ cm}^{-2}$.

^b Here “R” indicates *ROSAT* observations and “C” indicates *Chandra* observations.

^c Fluxes are for the energy range 0.5–10.0 keV and have been corrected for interstellar absorption.

^d The telescope was not dithered during the 2003 April 28 observation, resulting in a decrease in measured flux for those structures that were intersected by chip gaps and dead columns.

TABLE 2
DETECTED COUNT RATES AND FLUX FOR PSR B1509–58

Epoch	Total Count Rate ^a (counts s ⁻¹)	Hard Count Rate ^b (counts s ⁻¹)	Flux ^c (10 ⁻¹¹ ergs cm ⁻² s ⁻¹)
2000 Aug 14.....	0.130 ± 0.005	0.103 ± 0.005	5.0 ± 1.8
2003 Apr 21.....	0.144 ± 0.008	0.115 ± 0.008	5.1 ± 1.8
2003 Apr 28.....	0.138 ± 0.008	0.108 ± 0.008	5.1 ± 1.8
2003 Oct 18.....	0.142 ± 0.005	0.111 ± 0.005	5.2 ± 1.8

^a Count rates for the energy range 0.5–10.0 keV. They have been background-subtracted but have not been corrected for pileup. Errors are from Poisson statistics.

^b Count rates for the energy range 2.0–10.0 keV. They have been background-subtracted but have not been corrected for pileup. Errors are from Poisson statistics.

^c Fluxes for the energy range 0.5–10.0 keV, and they have been corrected for interstellar absorption and pileup. Uncertainties are all at 90% confidence. The models used are power laws of the form $f_E \propto E^{-\Gamma}$, where Γ is the photon index and has been held fixed at 1.19 (Cusumano et al. 2001) and where the integrated flux is $F_X \equiv F(E_1, E_2) = \int_{E_1}^{E_2} Ef(E) dE$. All models assume interstellar absorption using the cross sections of Bałucińska-Church & McCammon (1992), assuming solar abundances, with N_H held fixed at 8.6×10^{21} cm⁻². We have implemented the fast pileup algorithm of Davis (2001).

values do not significantly affect the fitted flux. This flux is within the error of that reported by G02. We conclude that the mismatch in our absorbing column and photon index values compared to the G02 results is most likely due to updated *Chandra* calibration solutions. Unless otherwise indicated, spectral fits in this paper hold N_H fixed at the simultaneous epoch fit value of 8.6×10^{21} cm⁻². Fluxes are reported for an energy range of 0.5–10.0 keV and have been corrected for interstellar absorption.

4.2. Flux of the Pulsar

To determine whether the pulsar flux has varied over time, we compared the background-subtracted count rate from a 1".4 radius region around the pulsar for each *Chandra* epoch over the energy ranges 0.5–10.0 and 2.0–10.0 keV. Note that these count rates do not reflect the true flux from the pulsar because of pileup. We chose the two different energy ranges to determine whether any variation in count rate could be due to pileup differences between epochs. A reduction in pileup might result from the extra absorption at low energies caused by the time-dependent ACIS filter contamination. The count rates are shown in Table 2. In 2000, the pulsar count rates between 0.5 and 10.0 keV and between 2.0 and 10.0 keV were ~8% less than in 2003, representing less than a 3 σ difference. Because the difference is approximately the same for the two energy ranges, it is unlikely that we have a significant bias from a reduction of pileup at low energies. We also determined the flux by performing a power-law fit to each of the *Chandra* data sets, correcting for interstellar absorption and pileup (Davis 2001). We held N_H fixed at 8.6×10^{21} cm⁻² and we held Γ fixed at 1.19 (Cusumano et al. 2001) for each epoch, but we allowed the normalization and the pileup grade morphing parameter to vary. As shown in Table 2, these fits indicate that the flux of the pulsar has remained steady at $\sim 5.1 \times 10^{-11}$ ergs cm⁻² s⁻¹.

4.3. Small-Scale Structure near the Pulsar

Figure 2 shows changes in the structure immediately surrounding the pulsar between 2000 August and 2003 October.⁶ In 2000, the structure consisted of four compact knots <3" across (corresponding to a physical size of 0.1–0.2 pc) located along the jet axis between distances of ~3" and 17" on both sides of the pulsar. Three years later, in 2003 April, this structure has

⁶ Note that the small-scale structure identified here was beyond the resolution capability of the *ROSAT* detectors.

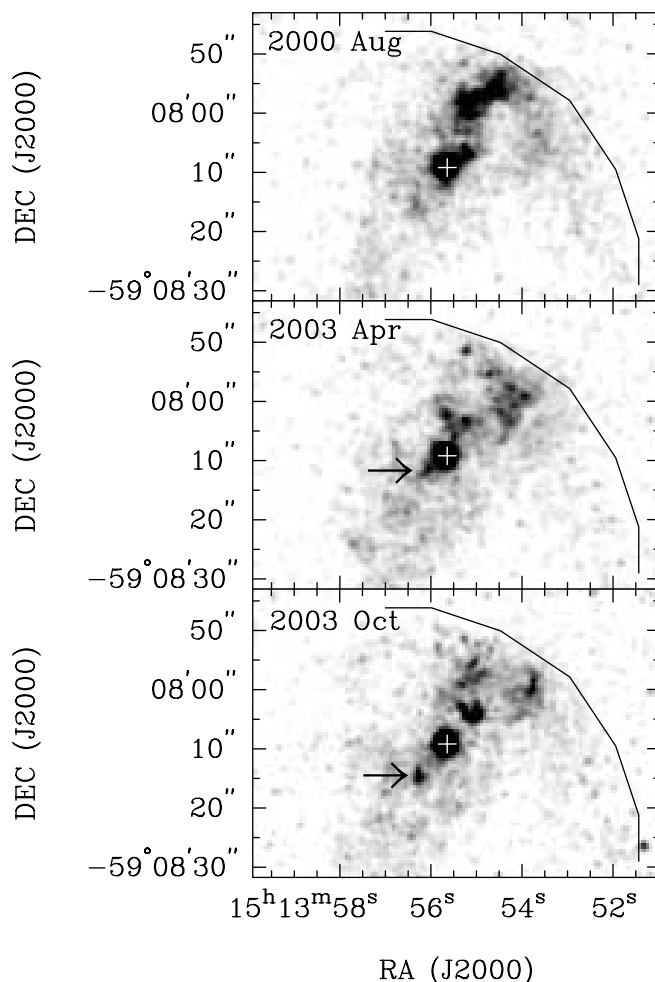


FIG. 2.—*Chandra* images showing changes in the environment immediately surrounding the pulsar. The 2003 April image combines both April observations. The images have been convolved with a Gaussian of FWHM 1". The energy range is 0.3–8.0 keV. The gray-scale range is linear and ranges from 0% to 3% of the peak value on all three images. The black arc indicates the location of the outer edge of the inner arc (see Fig. 1). Arrows on 2003 images indicate a possible knot in motion.

completely changed, with approximately nine small, unresolved knots ($<0''.5$, <0.01 pc) located along the jet axis between distances of $\sim 3''$ and $17''$ on both sides of the pulsar. No apparent changes were evident between 2003 April 21 and 2003 April 28. Approximately 6 months later, in 2003 October, the structure has again changed, with six knots ranging in size from $0''.5$ to $4''$, again located along the jet axis within $17''$ of the pulsar. In all cases, the knot activity is greater to the northwest than to the southeast, and in no case are knots found beyond the inner arc at a radius of $17''$.

There is the possibility that some of the knot variability we observe could be due to artifacts. It is known that artificial structures may appear near sources with strong pileup. However, we believe that most of the variability is real, because the typical count rates are ~ 0.005 – 0.05 counts s^{-1} (corresponding to 100–1000 counts on the 2000 August and 2003 October images), higher than would be expected for artificial structures. Another indication that the small-scale knots are genuine comes from our Monte Carlo simulations, which we discuss in § 4.5. In each of our 10 Poisson noise simulations, prior to smoothing to $10''$, we recover all of the knot structures. Furthermore, in analyzing their knot 1, G02 specifically ruled out asymmetries in the wings of the point-spread function and pulsar photons assigned to the wrong location on the sky as possible explanations. Finally, the small-scale knots are apparent on unsmoothed images and are not due to the $1''$ FWHM Gaussian convolution applied to Figure 2.

The knot structure changes so drastically that identifying motion is practically impossible. However, if the knot to the southeast of the pulsar in 2003 April and 2003 October is indeed the same feature (identified with arrows in Fig. 2), then the $4''$ motion results in a velocity of $\sim 0.6c$ (assuming outflow along the jet with a 30° inclination⁷ to the line of sight and correcting for relativistic Doppler boosting).

4.4. The Jet

We performed simultaneous absorbed power-law fits to the *ROSAT* PSPC and *Chandra* data for the jet in the same manner as we did for the diffuse PWN in § 4.1. We fixed N_H at 8.6×10^{21} cm^{-2} and required the same photon index for all the data sets, but we allowed the normalization to vary between epochs. The photon indices and fluxes are indicated in Table 1. As noted by G02, the photon index of the jet is flatter than that of the diffuse PWN. From the spectral fits, we note that the jet brightened by $\sim 30\%$ between the *ROSAT* PSPC observation in 1991/1992 and the *Chandra* observations; however, the flux remained steady from 2000 to 2003. The flux difference between the 1991/1992 *ROSAT* data and the 2000 *Chandra* data is slightly greater than the 90% confidence limit. This flux difference might be caused by the differing spectral responses of *ROSAT* and *Chandra*; however, this is presumably accounted for by the corresponding auxiliary response files. We can also exclude a systematic uncertainty in the calibration of the two observatories as contributing to the flux difference by examining the flux of the diffuse PWN. As seen in Table 1, the flux from the extended emission remains constant, as is expected.

We also compared the 1991/1992 *ROSAT* PSPC image, the 1994 *ROSAT* HRI image, and the 2000 August and 2003 October *Chandra* images of the jet, as shown in Figure 3. To facilitate comparison between different observatories that might arise from

the different responses of *ROSAT* and *Chandra*, the *Chandra* images are produced from events restricted to the 0.1–2.5 keV energy band of *ROSAT*. The resultant *Chandra* images, as well as the *ROSAT* HRI image, are then convolved with a Gaussian of FWHM $25''$ resolution to match the angular resolution of the *ROSAT* PSPC. Finally, to ensure that each data set has approximately the same number of total counts as the *ROSAT* PSPC and HRI observations, only a fraction of the *Chandra* observations were used to generate the images, as discussed in § 2. The images clearly show variability in the jet structure and brightness over a 12 yr period, supporting the flux measurements from the spectral fits. Indeed, the jet is dim and poorly defined in 1991/1992. In 1994, however, part of the jet structure $\sim 3'$ (corresponding to a distance of 9 pc, correcting for a jet inclination of 30° to the line of sight) to the southeast of the pulsar has brightened over the 2 yr since the previous observation. By 2000, the jet is well defined, with structure extending $4'$ from the pulsar, and it has a curved appearance. The 2003 *Chandra* observation shows that part of the jet $\sim 1'$ to the southeast of the pulsar has dimmed and that the structure at the end of the jet has become less well defined. The persistence of the inner and outer arc structures during the entire time range, taken with variability of the jet structure and relative intensity, indicates that the observed changes are in fact significant and real, since it is difficult to imagine an artifact that would only apply to discrete parts of the images. Hence, the jet brightening indicates the existence of an underlying mechanism, as we will discuss in § 6.2.

Despite remaining steady in total flux between 2000 and 2003, the jet shows variability on $\sim 20''$ size scales, as shown in Figure 4. In 2000, we identify four large ($20''$; physical size of 0.5 pc) clumps in the jet (labeled 1–4 in the top panel of Fig. 4) located between $\sim 1'$ (a separation from the pulsar of 3 pc at a 30° inclination) and $\sim 2.5'$ away from the pulsar. In 2003, there are two $\sim 20''$ -sized clumps located $\sim 1.5'$ and $1.7'$ away from the pulsar, with fainter emission further down the jet. If we interpret the clumps as the same structure having moved along the jet, then the velocity is $\sim 0.5c$ (assuming a 30° inclination to the line of sight and correcting for relativistic Doppler boosting). Due to the loss of dithering for the 2003 April 28 observation, we cannot determine whether the jet structure changed on week-long timescales. However, the 10 ks of data in the 2003 April 21 observation shows jet clumps with similar sizes and locations as those in the 2003 October observation, indicating that the jet structure changes on timescales longer than 6 months.

4.5. The Inner and Outer Arcs

ROSAT images indicated the presence of a cross-like structure around the pulsar (Brazier & Becker 1997). With the improved resolution of *Chandra*, the “cross” was resolved into inner and outer arcs (features “5” and “E” of G02) located approximately $17''$ and $40''$ (distances of 0.4 and 1.2 pc at a 60° inclination perpendicular to the jet) away from the pulsar. To determine whether the arcs have changed structure, we constructed *Chandra* and *ROSAT* HRI images that were matched in energy range, counts, and resolution to the *ROSAT* PSPC images, as described in § 2, § 4.4, and the caption of Figure 3. Due to the $\sim 25''$ resolution of the *ROSAT* PSPC detector, emission from the pulsar and small-scale knots surrounding the pulsar extends into the inner and outer arc structures. Therefore, we could not exclude the pulsar before smoothing without adversely affecting the arc structures. Figure 3 shows the comparison between the *ROSAT* and *Chandra* images. There appear to be structural changes to both the inner and outer arcs between 1991/1992, 1994, 2000, and 2003. In the same manner as for the diffuse PWN in § 4.1, we performed simultaneous

⁷ G02 derive a 30° jet inclination to the line of sight on the basis of Doppler boosting and radio polarization arguments, while Yatsu et al. (2005) derive an inclination angle $>50^\circ$ on the basis of an interaction between the unseen northwest jet and the RCW 89 region.

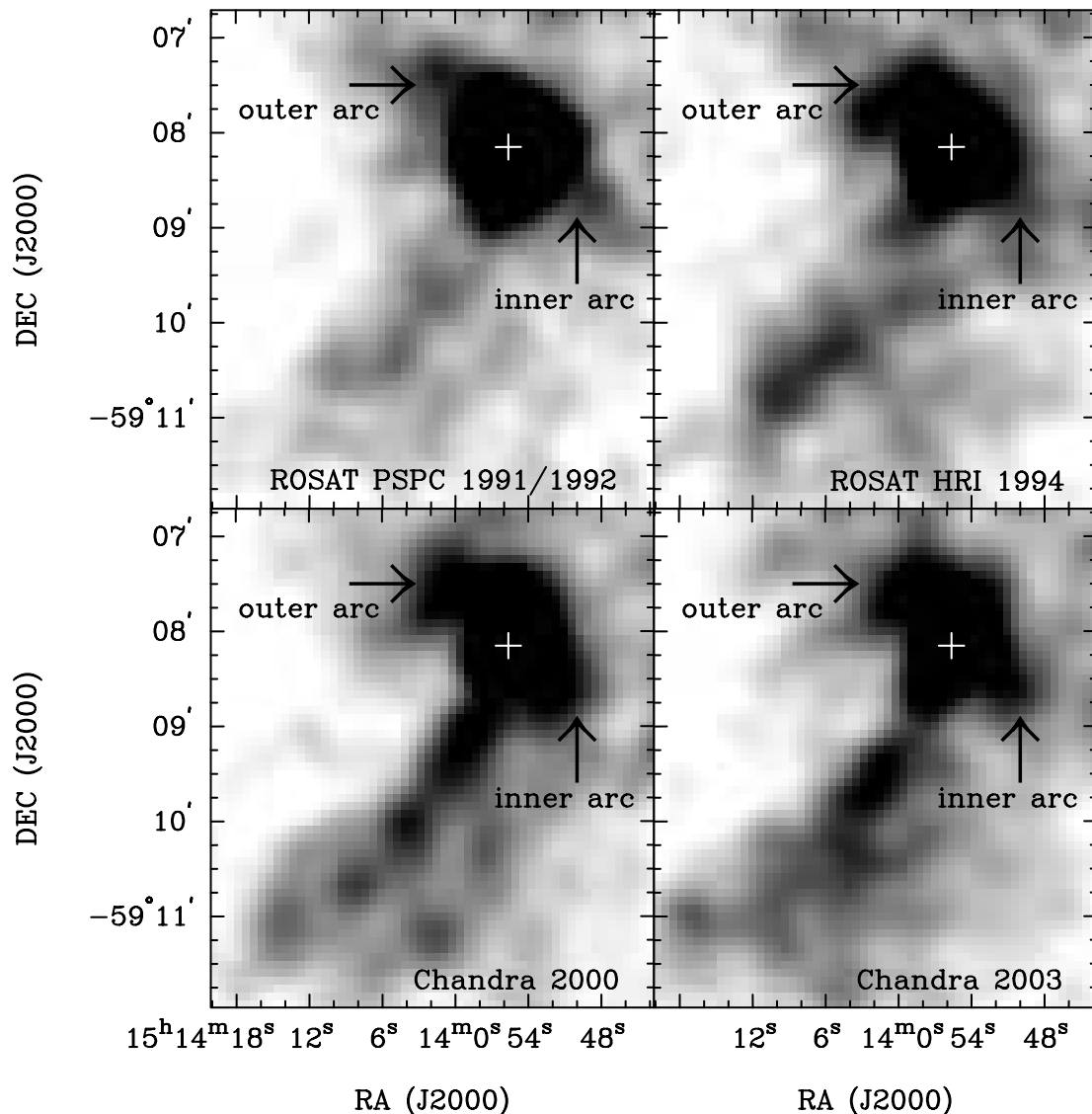


FIG. 3.—*Chandra* and *ROSAT* images showing changes in the outer arc and jet from 1991/1992 to 2003. To facilitate comparison between different observatories, the images are matched in resolution ($25''$), energy (0.5–10.0 keV), and counts, as described in §§ 2 and 4.4. The gray scale is linear and ranges from 2.2% to 13% of the peak value for the *ROSAT* PSPC and *Chandra* images and from 3.9% to 13% of the peak value on the *ROSAT* HRI image to account for the higher background of the HRI detector.

absorbed power-law spectral fits to the outer arc by using the *ROSAT* PSPC and *Chandra* data, holding N_{H} fixed at $8.6 \times 10^{21} \text{ cm}^{-2}$, requiring Γ to be the same for all the data sets, and allowing the normalization to vary between epochs. For the *Chandra* data, we reproduce the flux and photon index reported by G02, within the errors. As noted by G02, the outer arc has the same photon index as the jet, and the photon index is flatter than for the diffuse PWN. The outer arc appears to have *decreased* in brightness between 1991/1992 and 2000 by $\sim 20\%$, as shown in Table 1; however, this is only a 1σ result (68% confidence limit). This slight flux decrease may just be an artifact of the $\sim 25''$ resolution of the *ROSAT* PSPC detector and the pileup of the pulsar in the *Chandra* data (the low resolution of *ROSAT* results in pulsar counts contaminating the outer arc region, and the pileup of the pulsar with *Chandra* results in less contamination from the pulsar at the same resolution).

If we consider only the *Chandra* data, the outer arc shows time variability between 2000 August and 2003 October, as shown in Figure 5. In 2000 August, the outer arc contained two

major clumps, with the smaller clump having a $10''$ diameter and the larger clump elongated along the arc with a size of $10'' \times 20''$ ($0.25 \text{ pc} \times 0.5 \text{ pc}$). In 2003 October, the clump locations had changed within the outer arc, although the clump sizes were comparable to those of the 2000 clumps. Similar clump variability is also seen in the outer arc between 2003 April 21 and 2003 April 28, as shown in Figure 6, indicating that the timescale for arc variability might be as short as a few days. The white arrows in Figures 5 and 6 identify locations of transverse structural change between 2000 and 2003. Note that the changes observed in the outer arc between the 2003 April images are only slightly greater than one would expect from Poisson statistics. The greatest variation between the two 2003 April images, indicated by the rightmost arrow in Figure 6, is only 3σ on unsmoothed images. Spectral fits indicate that the total brightness of the outer arc has remained the same from 2000 to 2003.

The inner arc also shows a brightening to the west of the pulsar between 2000 and 2003, as seen in Figures 4 and 5; however, this is most likely due to the bright, pointlike source

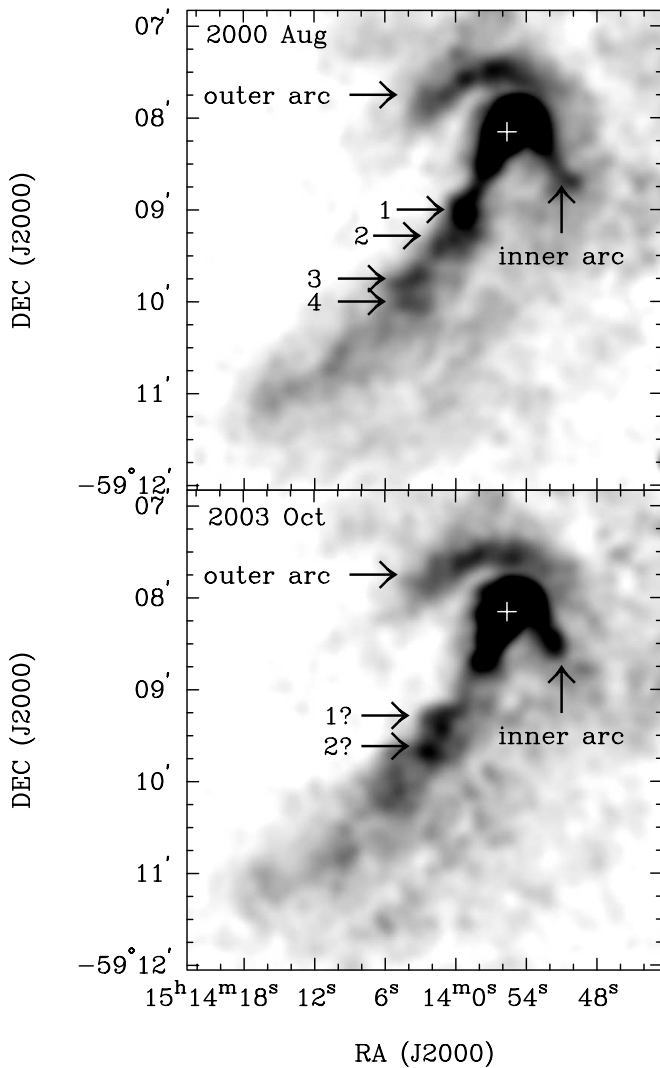


FIG. 4.—*Chandra* images convolved with a Gaussian of FWHM $10''$, showing changes in the jet. The numbers indicate the clumps as described in the text. The energy range is 0.3–8.0 keV. The gray scale is linear and ranges from 0.7% to 7% of the peak value.

near (J2000.0) R.A. = $15^{\text{h}}13^{\text{m}}51^{\text{s}}.5$, decl. = $-59^{\circ}08'25''$ in the 2003 October image, which can be seen most clearly in the bottom panel of Figure 2. A SIMBAD search shows no variable source in this location. While it is possible that this source could be related to the small-scale knots that we identified in § 4.3, we believe that it is more likely to be an artifact of a “hot pixel” in the data. The southwestern tip of the inner arc does appear to vary slightly between 2003 April 21 and 2003 April 28 (see Fig. 6); however, this may be due in part to the lower signal-to-noise ratio on the 10 ks exposures.

The inner and outer arcs were predicted to have outward motions of a few arcseconds per year (G02). To determine the proper motion of the outer arc, we convolved the 2000 August and 2003 October *Chandra* images with a Gaussian of FWHM $10''$. We then constructed an angle-averaged radial profile over the entire length of the outer arc and centered on the pulsar for each epoch, as shown in Figure 7. We measured the motion of the brightness profiles by minimizing χ^2 of the difference between the profiles at each epoch as a function of radial shift and amplitude scaling factor. We used data between radii of $38''$ and $55''$ (corresponding to the peak and outside edge of the brightness profiles) to measure the motion. It was necessary to use the

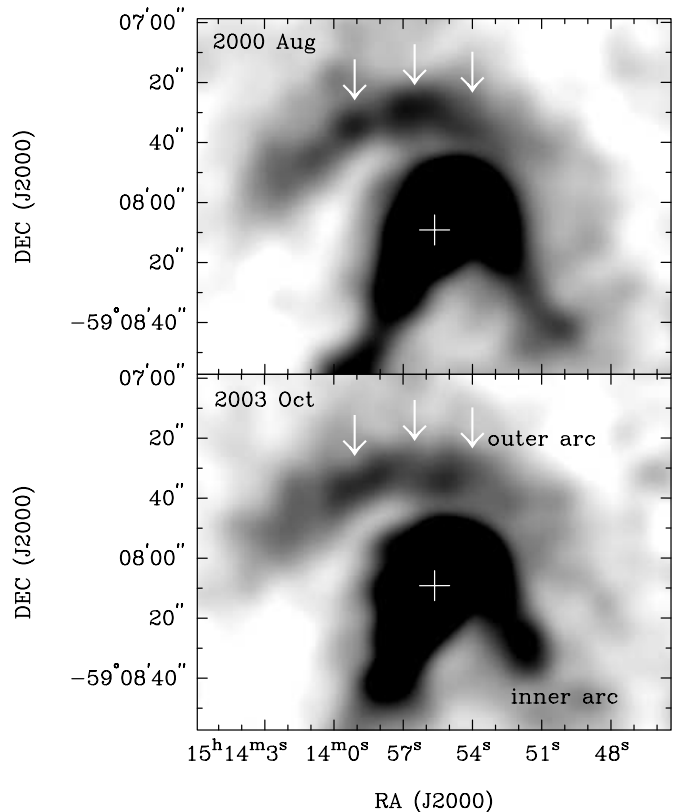


FIG. 5.—*Chandra* images convolved with a Gaussian of FWHM $10''$, showing changes in the inner and outer arcs over a 3 yr timescale. The white arrows indicate the locations of structural change between 2000 and 2003. The energy range is 0.3–8.0 keV, and the exposure time in each image is 20 ks. The gray scale is linear and ranges from 1.4% to 5.9% of the peak value.

peaks of the brightness profiles to break the degeneracy between motion and scaling differences between epochs. Data at radii less than $38''$ were excluded for the motion measurement because of the brightness variations caused by the small-scale knots near the inner arc. Although the small-scale knots are unresolved at $10''$ resolution, they do contribute significantly to the flux of the inner arc region. The error was determined at the 68% confidence limit of the χ^2 distribution. We confirmed the error by repeating the χ^2 measurement for 10 Monte Carlo simulations of the Poisson noise and calculating the rms scatter of the minimum χ^2 position. The outer arc appears to have moved *inward* by $1''.0 \pm 0''.2$ over the 3 yr time span from 2000 to 2003. This corresponds to a velocity of $0.03c$ (assuming outflow perpendicular to the jet with a 60° inclination to the line of sight and correcting for relativistic Doppler boosting). The convolution of the images and the angle averaging of the outer arc results in a measurement of the motion of the ensemble average of the material comprising the arc, which allows us to make a comparison to the model of G02. Thus, we can report that the average arc structure appears to move inward. However, given the degree of structural change in this time span, we cannot definitively determine whether this represents a real inward motion or is just a result of clump variation. We can rule out unaliased outward motion of the outer arc at the 5σ level. For the inner arc, there was too much structural change due to the nearby small-scale, compact knots to determine proper motions for that feature.

5. SPATIALLY RESOLVED SPECTROSCOPY

Although the jet structure has changed over the 3 yr time span of the *Chandra* observations, individual spectral fits to the 2000

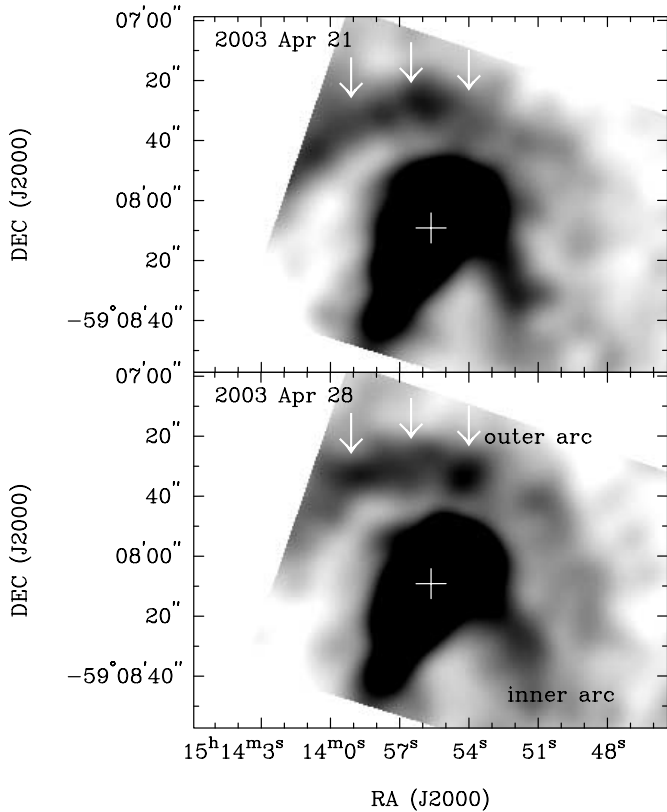


FIG. 6.—*Chandra* images convolved with a Gaussian of FWHM 10", showing changes in the inner and outer arcs over the span of a week. The white arrows are the same as in Fig. 5. The energy range is 0.3–8.0 keV, and the exposure time in each image is 10 ks. The gray scale is linear and ranges from 1.4% to 5.9% of the peak value. The images have been blanked to omit chip gap and dead column areas that could not be exposure-corrected in the 2003 April 28 observation.

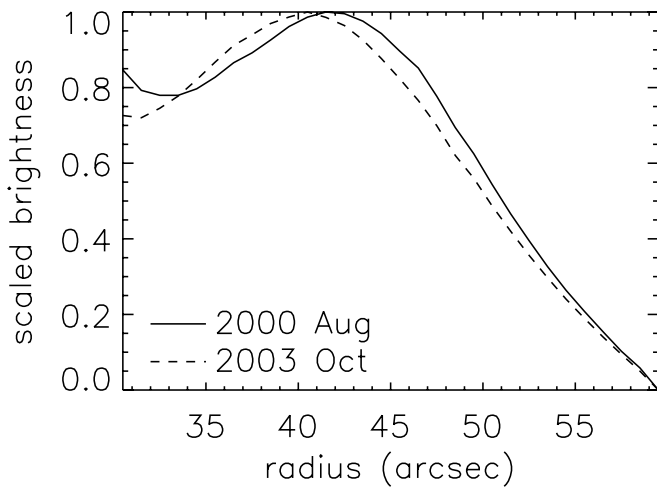


FIG. 7.—Angle-averaged radial profiles for the outer arc for the 2000 August and 2003 October *Chandra* images convolved with a Gaussian of FWHM 10". The difference in brightness at a radius of $\sim 31''$ – $32''$ is due to the variation of small-scale, compact knots near the inner arc between 2000 and 2003. Although the small-scale knots are unresolved at 10" resolution, they do contribute significantly to the flux of the inner arc region. Possible inward motion is indicated.

August and 2003 October data indicate that there was no photon index evolution in the jet and diffuse PWN during that time, as shown in Table 1. To determine whether the photon index of the diffuse PWN and the jet varied spatially, we used just the four *Chandra* data sets and performed simultaneous absorbed power-law fits, as outlined in § 4.1. For each region described below, we held N_{H} fixed to $8.6 \times 10^{21} \text{ cm}^{-2}$ and required the same Γ for all the data sets, but we allowed the normalization to vary between epochs.

For the diffuse PWN, we extracted spectra from concentric annuli 36" wide extending from a radius of 1/3 to 4/3, centered on the pulsar, as outlined in Table 3. The background region used for the diffuse PWN was a 36" wide annulus just exterior to the outermost "source" annulus and interior to the RCW 89 region. The background annulus was exterior to most of the PWN, except to the northwest and to the southeast, where it includes faint PWN emission. The jet was excluded from the diffuse PWN analysis. We performed a linear least-squares fit to determine the rate at which the photon index changed with radius. The results are shown graphically in Figure 8. The diffuse PWN shows a steepening of $0.04 \pm 0.02 \text{ arcmin}^{-1}$ between 1/3 and 3/1 (for a total $\Delta\Gamma$ of ~ 0.07) but flattens significantly thereafter. If we allow N_{H} to also vary for the diffuse PWN fits, the photon index does not flatten at large radii, and the best-fit slope is $0.08 \pm 0.02 \text{ arcmin}^{-1}$, which translates to a total change in photon index of 0.25 between 1/3 and 4/4. The value of N_{H} increases from $9.2 \times 10^{21} \text{ cm}^{-2}$ in the annulus closest to the pulsar to $13.2 \times 10^{21} \text{ cm}^{-2}$ in the annulus farthest from the pulsar. These values for the absorbing column are consistent with those derived by Trussoni et al. (1996), showing that there was about 1.5 times more absorption toward RCW 89 than toward the pulsar.

For the jet, we constructed five regions along the length of the jet, as shown in Figure 1. The separation from the pulsar was defined at the center of each region. The background for the jet analysis was chosen as the region immediately exterior to the total jet region. A linear least-squares fit was applied to the data and is shown in Figure 8. The jet shows a marginal photon index

TABLE 3
RADIAL VARIATIONS IN PHOTON INDEX FOR THE DIFFUSE PWN AND JET

Region	Distance (arcmin)	N_{H} (10^{21} cm^{-2})	Γ
Jet ^a	1.0	8.6 (fixed)	1.48 ± 0.27
	1.5		1.49 ± 0.26
	2.0		1.70 ± 0.16
	2.7		1.86 ± 0.24
	3.5		1.64 ± 0.45
Diffuse PWN ^b	1.3	8.6 (fixed)	1.84 ± 0.03
	1.9		1.91 ± 0.03
	2.5		1.88 ± 0.03
	3.1		1.93 ± 0.02
	3.7		1.84 ± 0.03
	4.3		1.74 ± 0.08
	Diffuse PWN.....	1.3	9.2 ± 0.5
	1.9	9.7 ± 0.5	2.02 ± 0.05
	2.5	10.3 ± 0.5	2.05 ± 0.05
	3.1	10.6 ± 0.6	2.14 ± 0.07
	3.7	10.9 ± 0.8	2.07 ± 0.09
	4.3	13.2 ± 1.4	2.18 ± 0.14

^a The regions used to extract spectra for the jet are shown in Fig. 1. Distances from the pulsar are measured at the geometric center of each region.

^b The regions used to extract spectra for the diffuse PWN are concentric annuli 36" wide. The radius is given at the center of each annulus. The jet region has been excluded from the diffuse PWN analysis.

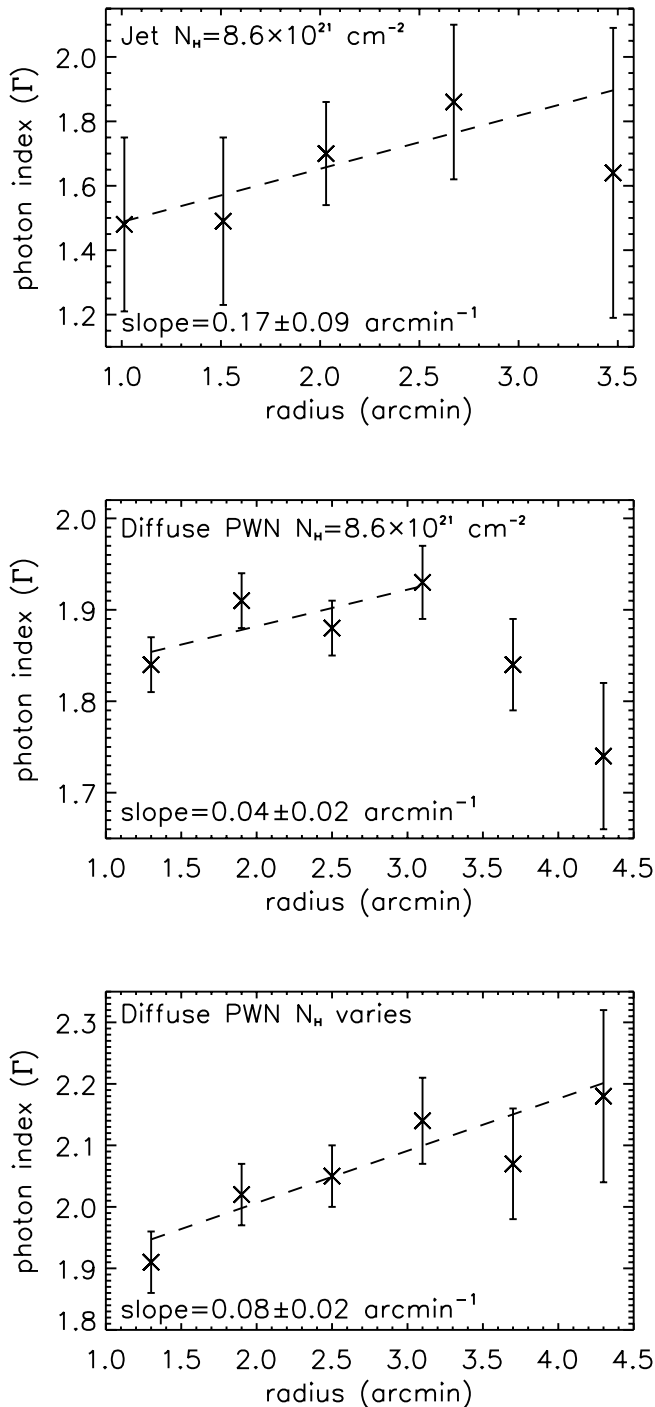


FIG. 8.—Plots of photon index vs. radius for the jet and diffuse PWN with linear least-squares fits (*dashed lines*), with the slope of the fit indicated. Error bars are shown for the 90% confidence limits.

steepening of $0.17 \pm 0.09 \text{ arcmin}^{-1}$ between radii of $1'$ to $3.5'$, for a total change of 0.43.

6. DISCUSSION

6.1. Variability of the Arcs

G02 suggested that the inner and outer arcs represent compressions downstream of the termination shock in an equatorial electron-positron pair outflow. The compressions are induced as the high-energy heavy ions (“protons”) embedded in the flow enter the shock-heated downstream pairs with the same velocity

and Lorentz factor as the upstream pair wind. This was an application of the model advanced by Gallant & Arons (1994) for the time-variable wisps seen in the termination shock region of the Crab Nebula, which has been shown by Spitkovsky & Arons (2004, hereafter SA04) to give a good representation of the structure and the toroidally averaged variations seen in the inner X-ray ring, as well as the propagating wave structures emerging from that ring as seen by *Chandra* (Hester et al. 2002). In the application of that model to G320.4–1.2, the inner and outer arcs were interpreted as the turning points in the orbits of the ions as they do their first gyrations in the shock-compressed magnetic field. Fitting the model to the G02 observations of G320.4–1.2 led to an estimate of the pair flux, upstream flow Lorentz factor, ion flux, and magnetic field in the equatorial flow. From that, G02 derived an ion cyclotron time on the order of 1–2 yr, which is the basic variability time of the ion-induced compressions. If all of the variation is in the form of bulk motion, the predicted outflow velocity from G02 is $\sim 0.5c$. Although our observations do not show an outward velocity, we do confirm the theoretical prediction of the variability timescale expected in the inner and outer arcs. That model, which is a toroidal average, did not predict the angular structure of the arcs uncovered by the new data presented here.

This model depends on the existence of ultra-high-energy heavy ions being present in the equatorial flow, with the ions carrying a large enough fraction of the energy flux to be able to induce substantial compression in the radiating pair plasma. The inferred ion number flux, both in the Crab Nebula and in G320.4–1.2, is approximately what one expects on electrodynamic grounds, if the ion stream is the electric return current required to prevent the charging up of the neutron stars. It is not currently understood how the particles in the flow achieve their high energies ($\gamma \sim 10^6$), although it has been suggested that they are accelerated and heated by the mysterious dissipation processes that lead to the equatorial wind having magnetization as weak as has been inferred (SA04 and references therein).

These kinetic models focus on the time-dependent morphology in and around the termination shock in the pairs; in effect, the ions form part of a resolved shock structure whose basic form is an equatorial ring. The large-scale structure of the nebular flow has been addressed in a series of MHD models and simulations, whose focus is on understanding the dramatic pole-to-equator asymmetry, especially the appearance of the jets (Bogovalov & Khangoulia 2002; Lyubarsky 2002; Komissarov & Lyubarsky 2003, 2004; Del Zanna et al. 2004; Bogovalov et al. 2005). These models assume that all the particles have small Larmor radius and thus are indifferent to composition and exclude the proposed high-energy ions by assumption. With the premise that the injected energy flux decreases with increasing rotational latitude θ (usually assumed proportional to $\cos^2\theta$), the energy is mostly injected through a higher latitude “arch shock,” which, because the shock is oblique to the flow, does not decelerate the plasma to subsonic speeds. These non-spherically symmetric shock structures can create the appearance of an inner ring of emission, with the weakly decelerated plasma emerging from the arch shocks contributing to the formation of the appearance of an outer ring. Doppler boosting may yield an appearance of partial arcs rather than complete rings.⁸

⁸ However, such a model then has difficulty explaining why the inner X-ray ring in the Crab Nebula has an approximately axisymmetric appearance, after toroidally averaging over the knots in the ring brightness, while the larger radius torus does show signs of Doppler boost. The ion compression model has the same difficulty. One of the major successes of the MHD model has been to find a flow that does have substantial Doppler boost at distances from the pulsar comparable to the Crab torus.

These models provide a plausible scenario for the formation of the jets as the consequence of backflow and magnetic hoop stress at higher latitudes.

The simulations of this model show no signs of short time variability corresponding to the wisps.⁹ The simulations may lack sufficient resolution to find the Kelvin-Helmholtz instability between the outward flow emerging from the arch shock and the higher latitude backflow, an effect suggested by Begelman (1999), with a somewhat different flow geometry in mind as the origin of the wisps. Alternatively, magnetization high enough to form the jet may suppress the shear flow instabilities.

While the effects of high-energy equatorial ions have not been explicitly included in the MHD simulations, if present, they would be injected into the shock-decelerated pairs through the equatorial ring shock seen in the MHD simulations. Thus, the formation of ion-driven compressions is qualitatively consistent with the MHD models and remains the only quantitatively elaborated model for the time variability seen in the Crab wisps and perhaps seen in the data described here. On the basis of this model, G02 predicted arc motions of a few arcseconds per year. We see no outward motion of the outer arc and perhaps even an inward motion. SA04 noted that the positions of the ion-driven compressions can move inward as well as outward, with the apparent motion then depending on when one takes a snapshot of the structure; the possible existence of apparent inward motion, perhaps seen in our data, is a prediction of the model. However, the apparent motion may also be due to the transverse structural variations in the outer arc between 2000 and 2003; nonaxisymmetric variability, a three-dimensional effect, has not been included in any of the models published to date. If such transverse change is the origin of the apparent motion, the arcs would then be quasi-stationary in the radial sense. Alternately, we could be witnessing aliasing as seen by Scargle (1969) in his observations of the wisps in the Crab Nebula, due to the observations having undersampled the variations.

We can test whether the quasi-stationary nature of the outer arc is due to aliasing. If we assume that the particles that comprise the outer arc are relativistic and thus Doppler boosted, then we can determine a speed on the basis of the brightness ratio of ≥ 5 between the near and far sides. For a photon index of 1.6, the Doppler-boosting formula reduces to $\beta \cos \phi = 0.22$, where $\beta = v/c$ and ϕ is the inclination angle to the line of sight. If the inclination of the outer arc is 60° (oriented 90° from the jet), then $\beta = 0.44$. At this speed, we expect the outer arc to move nearly $16''$ in 3 yr, which is slightly greater than the width of the arc. Over 6 months, the outer arc should move $2''$ – $3''$, which is not observed. Suppose that the motion of particles *through* the arc is not indicative of the motion of the arc. In this case, consider that the arc would need to move at $0.27c$ to move its width (0.25 pc) in 3 yr. At this speed, the arc would only move $1.6''$ in 6 months. This amount of motion is difficult to rule in or out, given the degree of structural change in the outer arc and the signal-to-noise ratio of the data.

The nature of arc a and arc b is unknown. If indeed the arcs are outward-moving structures, then perhaps arc a and arc b are just more evolved versions of the inner and outer arcs. They could also represent a quasi-coherent oscillation of the flow in the outer PWN, as observed in the simulations of Bogovalov et al. (2005).

⁹ Bogovalov et al. (2005) do report a long-period quasi-coherent oscillation of the flow ($t \sim 40$ yr) with some possible shorter time variability when the magnetization is finite but not large; the variability vanishes for unmagnetized flow models. The physical reasons for this variability are not understood (S. V. Bogovalov 2005, private communication).

TABLE 4
ALFVÉN CROSSING TIMES IN THE JET

Position ^a	B_{\min} (μG)	U_{\min} (10^{-11} ergs cm^{-3})	t_A^b (yr)
1.....	15	2.1	1.3
2.....	17	2.8	1.3
3.....	14	1.7	2.0
4.....	12	1.3	2.0
5.....	11	1.1	1.6

^a Positions are shown in Fig. 1; position 1 is closest to the pulsar. Volumes at each position are assumed to be cylindrical.

^b The Alfvén velocity at each position along the jet as computed from eq. (1) is $\approx 0.63c$.

A more thorough analysis of these faint PWN structures will be performed at a later time.

6.2. Variability in the Jet

MHD sausage or kink instabilities are viable candidates for the jet variability, as in the Vela jet (Pavlov et al. 2003). The timescale for such phenomena is set by the Alfvén crossing time $t_A = r_{\text{jet}}/v_A$, where r_{jet} is the cylindrical radius of the jet and

$$v_A = \frac{c}{\sqrt{1 + [4\pi(\rho c^2 + 4p)]/B^2}} \approx \frac{c}{\sqrt{1 + (16\pi U/3B^2)}}. \quad (1)$$

Here p is the relativistic pressure, assumed to be isotropic, and $U = 3p \gg \rho c^2$ is the energy density of the relativistic plasma. Shown in Table 4 are the magnetic fields, plasma energy densities, and Alfvén crossing times for regions along the jet as shown in Figure 1. Position 1 is closest to the pulsar, and we assume a cylindrical volume. The magnetic fields and energy densities are computed from equipartition arguments, using integrated fluxes for the energy range 0.5–10 keV and assuming an uncooled spectrum (Pacholczyk 1970, pp. 170–171). For all regions, $v_A \approx 0.63c$, and the Alfvén crossing times vary from 1.3 to 2 yr. Thus, the MHD instability of a magnetic pinch, the basic structure of the jet described in the MHD models, certainly is a viable candidate for the jet variations observed between 2000 and 2003 and perhaps may be a candidate to explain the partial brightening of the jet from 1991/1992 to 1994 and 2000. Indeed, episodic jet outflows are observed in MHD simulations for certain magnetic field configurations (Ouyed et al. 1997; Ouyed & Pudritz 1997).

If we interpret the jet structural changes between 2000 and 2003 as clump motion along the jet, then the resulting velocity is $\sim 0.5c$. This velocity is consistent with the prediction of G02 based on Doppler boosting and also matches the outflow speeds observed in the Crab Nebula jet ($0.4c$; Hester et al. 2002), the Vela PWN jet ($0.3c$ – $0.7c$; Pavlov et al. 2003), and in the jet of G11.2–0.3 ($0.8c$ – $1.4c$; Roberts et al. 2003). Relativistic jet outflow velocities of $\sim 0.5c$ are predicted by the MHD simulations described above (Bogovalov et al. 2005; Del Zanna et al. 2004; Komissarov & Lyubarsky 2003, 2004). The jet brightening from 1991/1992 to 1994 and 2000 cannot simply be a result of material moving at $0.5c$ down the jet, causing the jet to lengthen and brighten with the inclusion of more material. This scenario is excluded for two reasons: the first is that it would take nearly 80 yr for material moving at $0.5c$ to travel the length of the jet, and the second is that the jet seems to brighten in a “patchy” manner and does not simply lengthen, as shown in Figure 3. Therefore, as discussed above, the brightening of the jet is more

likely the result of an MHD instability such as a magnetic pinch. In this model, the instability causes compression and brightening of local regions, each of which has a length of no more than the jet diameter. There is no necessity for the energy to be injected into the jet at a varying rate, with the observed variations reflecting transport along the jet. This scenario works because the Alfvén transit time *across* the jet is much shorter than the flow time along the jet. The model suggests that the clumps vary incoherently with respect to each other, on a timescale approximately equal to the Alfvén crossing time (< 2 yr), consistent with the very limited time series available to us.

6.3. Small-Scale Structure near the Pulsar

The compact, small-scale knots near the pulsar are quite variable on 6 month timescales. Although the knot to the southeast of the pulsar might represent material moving at $0.6c$, given the startling knot variability to the northwest, a conclusion of knot motion is perhaps premature. We can estimate the magnetic fields in the knots in three ways: (1) assume that the knot size is approximately the Larmor radius of gyrating pairs, (2) use equipartition, and (3) use the synchrotron lifetime if the knots are in motion at $0.6c$ and cool below detectability at a distance of the inner arc in time frames from 6 months to 1 yr. For the first method, G02 derived a magnetic field of $3 \mu\text{G}$ from the Larmor radius for their knot 1. For the second method, the magnetic field derived from minimum energy using a size of 0.1 pc and the integrated flux of knot 1 from G02 for the energy range of 0.5–10.0 keV is $B_{\text{min}} = 76 \mu\text{G}$. For the third method, the synchrotron lifetime can be calculated using (from eq. [4] of G02):

$$t_{\text{synch}} = 39B^{-3/2}\varepsilon^{-1/2} \text{ kyr}, \quad (2)$$

where B is the magnetic field in units of μG and ε is the energy in units of keV. For 5 keV and $t_{\text{synch}} = 1$ yr, $B = 700 \mu\text{G}$. Given this high magnetic field, it seems unlikely that synchrotron cooling could be responsible for the transient nature of the knots.

The knots may have a similar explanation as that for “knot 2” in the Crab Nebula, which has been interpreted as an unstable quasi-stationary shock in the polar jet outflow (Hester et al. 2002). In this scenario, one would expect the bulk of the knots to be in the approaching jet, since the receding jet is Doppler boosted down in brightness. However, in this case we observe most of the knot structure on the receding jet side.

Given that the knots are never observed beyond the inner arc radius and that most of them occur on the approaching side of the arcs, it is likely that the knots are either associated with the equatorial outflow or the resulting backflow, as was described in § 6.1 and is shown in Figure 3 of Komissarov & Lyubarsky (2003). Two processes expected from the relativistic MHD simulations that could produce “knotlike” emission are Kelvin-Helmholtz (KH) instabilities arising in the shear layer between the equatorial outflow and the backflow and unsteady vortices that develop in the converging flow at the base of the jet.

The KH instability creates waves that may grow and break while traveling in the direction of the mass-weighted jump in velocity across the interface between the outflow and backflow. Doppler boosting as the breaking waves head toward us, and plasma and B -field compression as the waves break, may lead to the formation of bright features that can appear to us as localized bright spots of emission. The main difficulty with this idea is that within the flow models, the mass-weighted velocity jump is directed toward us only on the near (visible jet) side, except very close in to the base of the jets. This is because flow convergence

increases the mass density in the layer that converges on the axis at small distances from the axis, while the outflowing layer has low density at small radii. At larger radii, the relative densities of the layers reverse. Thus, this effect will work only if there is a lot of flow convergence.

The converging flow at the base of the jet could also produce transient features due to the development of unstable vortices (N. Bucciantini 2005, private communication). The backflow would need to focus quite well toward the base of the jet to produce Doppler boosting of flows directed toward us and may be rather sensitive to the maintenance of axisymmetry. However, this hypothesis naturally explains the relative absence of knots on the near (visible) jet side, since the converging flow at the base of the approaching jet would be directed away from us.

Regardless of the actual cause of the knots, they seem to be diagnostic of flow details in the PWN. To determine the true nature of the knots will require much higher resolution simulations and more analysis of the flow models.

6.4. Synchrotron Cooling in the Jet and Diffuse PWN

G02 determined that the synchrotron cooling time for the jet at 5 keV and with a magnetic field of $\sim 25 \mu\text{G}$ is 140 yr. This cooling should result in a $\Delta\Gamma$ of 0.5 (Kardashev 1962; Pacini & Salvati 1973). Indeed, there is a marginal indication of cooling in the jet with a total $\Delta\Gamma$ of 0.43. We await analysis of the new, longer *Chandra* observation to verify the possible synchrotron cooling in the jet. The relativistic MHD simulations do predict that the jet should undergo synchrotron cooling, although there is mixing with the ambient PWN material (S. Komissarov 2005, private communication). At the base of the jet, the photon index should match that of the equatorial outflow, since the jet is constructed from purloined equatorial material. If we assume that the inner and outer arcs identify the equatorial outflow material, then their photon index of 1.6 does nearly match the photon index of 1.5 at the base of the jet. If the spectral steepening along the jet is real, it would be similar to that observed in the Crab Nebula jet ($\Delta\Gamma \sim 0.5$; Mori et al. 2004a).

Spectral steepening with increasing radius has been observed in a number of PWNe and is generally attributed to both synchrotron cooling and expansion losses (Gonzalez & Safi-Harb 2003; Lu et al. 2002; Mori et al. 2004a; Safi-Harb et al. 2001; Slane et al. 2004). The degree of steepening varies from $\Delta\Gamma \sim 0.3$ to 1.3 with a typical value of 1, and the radial photon index profiles generally show a monotonic increase with radius. Our spectral results for the diffuse component of the PWN of G320.4–1.2 also show a monotonic increase of photon index with radius if we allow the absorption to vary, but the degree of steepening (~ 0.25) is less than in other PWNe. In contrast, models for synchrotron cooling in PWNe based on the Kennel & Coroniti (1984) model predict a rapid increase in photon index at large radius (Reynolds 2005; Slane et al. 2004). Perhaps the discrepancy between the cooling model and the observations is due to large-scale mixing of recently accelerated material with “older” material, as predicted by the relativistic MHD models (Bogovalov & Khangoulouian 2002; Lyubarsky 2002; Komissarov & Lyubarsky 2003, 2004; Del Zanna et al. 2004; Bogovalov et al. 2005).

7. SUMMARY AND CONCLUSIONS

Variability is observed in the X-ray PWN of PSR B1509–58 on timescales possibly as short as 1 week and up to 12 yr. Our primary results are as follows:

1. The compact, small-scale knots appearing within $20''$ of the pulsar exhibit transient behavior that may be attributed to

turbulence in the flows surrounding the pulsar. Possible knot motion is indicated with a velocity of $0.6c$.

2. Apparent outflow along the jet is observed with velocities of $\sim 0.5c$. This outflow alone cannot account for the $\sim 30\%$ brightening of the jet between 1991/1992 and 2000. The Alfvén crossing time for the jet is 1.3–2 yr; therefore, MHD kink or sausage instabilities could account for the rapid morphological variations and perhaps the partial jet brightening.

3. The outer arc has possibly moved inward with a velocity of $0.03c$; however, the transverse structural changes seen in the outer arc may account for the apparent motion. We cannot determine at this time if the outer arc is truly quasi-stationary or if we are witnessing aliasing.

4. The diffuse PWN has not evolved significantly in structure or brightness over the 12 yr time span. Using the summed *Chandra* images, we identify two possible arc structures exterior to the outer arc.

5. The photon indices of the diffuse PWN and possibly the jet steepen with increasing radius, indicating synchrotron cooling at X-ray energies.

Although our imaging capabilities have improved substantially since the first optical observations of time variability in the Crab Nebula (Scargle 1969), our understanding of these variations in PWNs is still quite limited. For instance, while we expect magnetic fields to play an important dynamical role in jets, and indeed we do see variations on the appropriate Alfvén crossing times, we do not know for certain whether MHD instabilities are the root cause of the observed variations. The arc structures that we observe in G320.4–1.2 are equally enigmatic. We do not

yet know if they are in steady motion or are quasi-stationary wave phenomena. The striking changes in the small-scale knots near the pulsar may simply be “weather,” diagnosing unimportant details in the PWN flow, or they may indicate important flow structure that is essential to understanding, for instance, the diffusion of particles from the equatorial flow to higher latitudes, a loss essential to a post-pair shock second-order Fermi acceleration model. Certainly, deeper and appropriately spaced X-ray observations will help resolve some issues, such as the possible spatial aliasing of the outer arc. Also, the higher signal-to-noise ratios will provide better constraints on the spatial spectral index variations and allow us to determine if and how much mixing has occurred in the diffuse PWN. Finally, we are excited by the recent development of relativistic MHD models, and we hope that some of the variability we observe here can eventually be observed in those simulations.

We thank Fred Seward for assistance with *ROSAT* data analysis, Elena Amato, Niccolò Bucciantini, and Serguei Komissarov for helpful discussions, and the anonymous referee for a careful reading of the manuscript. This research has made use of data obtained from the High Energy Astrophysics Science Archive Research Center (HEASARC), provided by NASA’s Goddard Space Flight Center. T. D. and B. M. G. acknowledge the support of NASA through SAO grant GO3-4063A. J. A. acknowledges support from NASA *Chandra* theory grant TM4-5005X, from NASA ATP grant NAG5-12031, and from the taxpayers of California.

REFERENCES

- Aharonian, F., et al. 2005, *A&A*, 435, L17
 Bałucińska-Church, M., & McCammon, D. 1992, *ApJ*, 400, 699
 Begelman, M. C. 1999, *ApJ*, 512, 755
 Bietenholz, M. F., Hester, J. J., Frail, D. A., & Bartel, N. 2004, *ApJ*, 615, 794
 Bogovalov, S. V., Chechetkin, V. M., Koldoba, A. V., & Ustyugova, G. G. 2005, *MNRAS*, 358, 705
 Bogovalov, S. V., & Khangoulouian, D. V. 2002, *MNRAS*, 336, L53
 Brazier, K., & Becker, W. 1997, *MNRAS*, 284, 335
 Cusumano, G., Mineo, T., Massaro, E., Nicastro, L., Trussoni, E., Massaglia, S., Hermsen, W., & Kuiper, L. 2001, *A&A*, 375, 397
 Davis, J. E. 2001, *ApJ*, 562, 575
 Del Zanna, L., Amato, E., & Bucciantini, N. 2004, *A&A*, 421, 1063
 Gaensler, B. M., Arons, J., Kaspi, V. M., Pivovarov, M. J., Kawai, N., & Tamura, K. 2002, *ApJ*, 569, 878 (G02)
 Gaensler, B. M., Brazier, K. T. S., Manchester, R. N., Johnston, S., & Green, A. J. 1999, *MNRAS*, 305, 724
 Gallant, Y. A., & Arons, J. 1994, *ApJ*, 435, 230
 Gonzalez, M., & Safi-Harb, S. 2003, *ApJ*, 583, L91
 Greiveldinger, C., Caucino, S., Massaglia, S., Ögelman, H., & Trussoni, E. 1995, *ApJ*, 454, 855
 Helfand, D. J., Gotthelf, E. V., & Halpern, J. P. 2001, *ApJ*, 556, 380
 Hester, J. J., et al. 1995, *ApJ*, 448, 240
 ———. 2002, *ApJ*, 577, L49
 Jerius, D., Donnelly, R. H., Tibbetts, M. S., Edgar, R. J., Gaetz, T. J., Schwartz, D. A., Van Speybroeck, L. P., & Zhao, P. 2000, *Proc. SPIE*, 4012, 17
 Kardashev, N. S. 1962, *Soviet Astron.*, 6, 317
 Kaspi, V., Manchester, R., Siegman, B., Johnston, S., & Lyne, A. 1994, *ApJ*, 422, L83
 Kennel, C. F., & Coroniti, F. V. 1984, *ApJ*, 283, 694
 Komissarov, S. S., & Lyubarsky, Y. E. 2003, *MNRAS*, 344, L93
 ———. 2004, *MNRAS*, 349, 779
 Livingstone, M. A., Kaspi, V. M., Gavriil, F. P., & Manchester, R. N. 2005, *ApJ*, 619, 1046
 Lu, F. J., Wang, Q. D., Aschenbach, B., Durouchoux, P., & Song, L. M. 2002, *ApJ*, 568, L49
 Lyubarsky, Y. E. 2002, *MNRAS*, 329, L34
 Melatos, A., Scheltus, D., Whiting, M. T., Eikenberry, S. S., Romani, R. W., Rigaut, F., Spitkovsky, A., Arons, J., & Payne, D. J. B. 2005, *ApJ*, 633, 931
 Mori, K., Burrows, D. N., Hester, J. J., Pavlov, G. G., Shibata, S., & Tsunemi, H. 2004a, *ApJ*, 609, 186
 Mori, K., Burrows, D. N., Pavlov, G. G., Hester, J. J., Shibata, S., & Tsunemi, H. 2004b, in *IAU Symp.* 218, *Young Neutron Stars and Their Environments*, ed. F. Camilo & B. M. Gaensler (San Francisco: ASP), 181
 Muzzio, J. C. 1979, *AJ*, 84, 639
 Ouyed, R., & Pudritz, R. 1997, *ApJ*, 484, 794
 Ouyed, R., Pudritz, R., & Stone, M. 1997, *Nature*, 385, 409
 Pacholczyk, A. G. 1970, *Radio Astrophysics* (San Francisco: Freeman)
 Pacini, F., & Salvati, M. 1973, *ApJ*, 186, 249
 Pavlov, G. G., Kargaltsev, O. Y., Sanwal, D., & Garmire, G. P. 2001, *ApJ*, 554, L189
 Pavlov, G. G., Teter, M. A., Kargaltsev, O., & Sanwal, D. 2003, *ApJ*, 591, 1157
 Pfeffermann, E., et al. 1987, *Proc. SPIE*, 733, 519
 Reynolds, S. P. 2005, in *IAU Colloq.* 192, *Cosmic Explosions: On the 10th Anniversary of SN 1993J*, ed. J. M. Marcaide & K. W. Weiler (Berlin: Springer), posters supplement, 161
 Roberts, M. S., Tam, C. R., Kaspi, V. M., Lyutikov, M., Vasisht, G., Pivovarov, M., Gotthelf, E. V., & Kawai, N. 2003, *ApJ*, 588, 992
 Rodgers, A. W., Campbell, C. T., & Whiteoak, J. B. 1960, *MNRAS*, 121, 103
 Safi-Harb, S., Harrus, I. M., Petre, R., Pavlov, G. G., Koptsevich, A. B., & Sanwal, D. 2001, *ApJ*, 561, 308
 Scargle, J. D. 1969, *ApJ*, 156, 401
 Seward, F. D., Harnden, F. R., Jr., Murdin, P., & Clark, D. H. 1983, *ApJ*, 267, 698
 Slane, P., Helfand, D. J., van der Swaluw, E., & Murray, S. S. 2004, *ApJ*, 616, 403
 Spitkovsky, A., & Arons, J. 2004, *ApJ*, 603, 669 (SA04)
 Trümper, J. 1982, *Adv. Space Res.*, 2, 241
 Trussoni, E., Massaglia, S., Caucino, S., Brinkman, W., & Aschenbach, B. 1996, *A&A*, 306, 581
 Weisskopf, M. C., et al. 2000, *ApJ*, 536, L81
 Yatsu, Y., Kawai, N., Kataoka, J., Kotani, T., Tamura, K., & Brinkmann, W. 2005, *ApJ*, 631, 312